



# Mesoporous $\text{PbI}_2$ assisted growth of large perovskite grains for efficient perovskite solar cells based on ZnO nanorods



Shibin Li <sup>a,\*</sup>, Peng Zhang <sup>a</sup>, Hao Chen <sup>a</sup>, Yafei Wang <sup>a</sup>, Detao Liu <sup>a</sup>, Jiang Wu <sup>c</sup>,  
Hojjatollah Sarvari <sup>b</sup>, Zhi David Chen <sup>a,b,\*\*</sup>

<sup>a</sup> State Key Laboratory of Electronic Thin Films and Integrated Devices, School of Optoelectronic Information, University of Electronic Science and Technology of China (UESTC), Chengdu, 610054, China

<sup>b</sup> Department of Electrical & Computer Engineering and Center for Nanoscale Science & Engineering, University of Kentucky, Lexington, KY, 40506, USA

<sup>c</sup> Department of Electronic and Electrical Engineering, University College London, Torrington Place, London, WC1E 7JE, United Kingdom

## HIGHLIGHTS

- Mesoporous  $\text{PbI}_2$  films are prepared by two-step annealing.
- Mesoporous  $\text{PbI}_2$  assisted the growth of large perovskite grains.
- Perovskite solar cells based on ZnO nanorods yield high efficiency of 17.3%.

## ARTICLE INFO

### Article history:

Received 9 December 2016

Accepted 4 January 2017

### Keywords:

Perovskite solar cell

ZnO nanorods

Carrier recombination

Mesoporous  $\text{PbI}_2$

## ABSTRACT

Perovskite solar cells (PSCs) have attracted great attention due to their low cost and high power conversion efficiency (PCE). However, the defects and grain boundaries in perovskite films dramatically degrade their performance. Here, we show a two-step annealing method to produce mesoporous  $\text{PbI}_2$  films for growth of continuous, pinhole-free perovskite films with large grains, followed by additional ethanol vapor annealing of perovskite films to reduce the defects and grain boundaries. The large perovskite grains dramatically suppress the carrier recombination, and consequently we obtain ZnO-nanorod-based PSCs that exhibit the best efficiency of 17.3%, with high reproducibility.

© 2017 Elsevier B.V. All rights reserved.

## 1. Introduction

Thanks to various attractive optoelectronic characteristics, including a high absorption coefficient, a tunable bandgap, and a long carrier diffusion length, the family of perovskite materials are ideal light harvesters [1–12]. Methylammonium lead iodide ( $\text{MAPbI}_3$ ), with a bandgap of about 1.5 eV and a light absorption spectrum up to a wavelength of 800 nm, has been extensively studied as a light harvester in solar cells. Following a rapid surge of development, solution processed  $\text{MAPbI}_3$  has boosted the power conversion efficiency (PCE) of perovskite solar cells (PSCs) based on

ZnO to above 17% [13] and  $\text{TiO}_2$  to above 22% [14]. Most of PSCs based on  $\text{TiO}_2$  electron transporting materials (ETM), but ZnO attracts attention for using as ETM in PSCs due to its high electron mobility.

The performance of PSCs depends strongly on crystalline quality and morphology of  $\text{MAPbI}_3$  films. The two-step sequential method is widely adopted for deposition of perovskite films. However, the sequentially deposited perovskite film suffers from lower crystallinity as compared to those produced from the one-step solution method. A great deal of efforts, for instance, thermal annealing, vapor assisted perovskite formation, solvent additives, and mixed solvents for preparation of perovskite precursors have been carried out to improve the crystalline quality of sequentially deposited  $\text{MAPbI}_3$  films [15–17]. Among these methods, solvent vapor annealing is one of the most effective and facile ways to improve the crystal morphology of  $\text{MAPbI}_3$  [18–23]. The goal of these studies is to fabricate a compact perovskite film with large grains. Regarding solvent annealing (SA) processes, most works focused on

\* Corresponding author.

\*\* Corresponding author. State Key Laboratory of Electronic Thin Films and Integrated Devices, School of Optoelectronic Information, University of Electronic Science and Technology of China (UESTC), Chengdu, 610054, China.

E-mail addresses: [shibinli@uestc.edu.cn](mailto:shibinli@uestc.edu.cn) (S. Li), [zhichen@engr.uky.edu](mailto:zhichen@engr.uky.edu) (Z.D. Chen).

annealing perovskite films in solvent atmospheres, for example DMF, DMSO, methanol, ethanol, pyridine, and isopropanol. Most of the solvent annealing processes treated perovskite films themselves, but formation of sequentially deposited perovskite films also strongly depends on the surface morphology of  $\text{PbI}_2$  films. Wong et al. demonstrated that porous  $\text{PbI}_2$  contributes to full conversion of  $\text{PbI}_2$  to  $\text{MAPbI}_3$ , resulting in a  $\text{PbI}_2$ -free and highly oriented perovskite film [24]. Zhu and the coworkers reported the use of mesoporous  $\text{PbI}_2$  as scaffold for highly efficient planar heterojunction PSCs [25]. Based on mesostructured lead halide, Graetzel et al. produced contiguous and dense perovskite films consisting of  $\text{FA}_{1-x}\text{MA}_x\text{Pb}(\text{I}_{1-x}\text{Br}_x)_3$  for high performance PSCs [26]. The above studies demonstrated that porous  $\text{PbI}_2$  films facilitate crystallization and grain growth of perovskite films. Recently, we employed an effective solvent annealing process for  $\text{PbI}_2$  films, and sequentially prepared high quality perovskite films. The obtained  $\text{TiO}_2$ -based PSCs exhibited an efficiency of 18.5% [27].

In this paper, we present a new approach for producing high quality perovskite films with large grains on ZnO nanorods (NRs). The mesoporous  $\text{PbI}_2$  film was prepared by a two-step thermal annealing method from  $\text{PbI}_2$  in a mixed solution of N,N'-dimethylformamide (DMF) and dimethyl sulfoxide (DMSO). The prepared mesoporous  $\text{PbI}_2$  films assisted the growth of large grains in sequentially deposited perovskite films. The perovskite films were then solvent annealed in the ethanol vapor atmosphere to further increase the compactness and grain size. As a result, the attained efficiency of PSCs based on ZnO NRs is as high as 17.3%.

## 2. Experimental

### 2.1. Fabrication of ZnO NRs based perovskite solar cells

The schematic flow diagram shown in Fig. 1 exhibits fabrication processes of PSCs based on ZnO NRs. ZnO NRs based PSCs were fabricated by using a two-step method in a nitrogen-filled glove box ( $<1$  ppm  $\text{O}_2$  and  $\text{H}_2\text{O}$ ). A hydrothermal method was employed to grow ZnO NRs at  $90^\circ\text{C}$  on a thin ZnO film (30 nm) seed layer prepared at room temperature on fluorine-doped tin oxide (FTO) coated glasses. Atomic layer deposition of  $\text{Al}_2\text{O}_3$  monolayers passivated the surface of ZnO NRs. The  $\text{PbI}_2$  solution (460 mg/mL) was prepared by dissolving  $\text{PbI}_2$  at  $70^\circ\text{C}$  in DMF, DMSO, and an optimized mixture solution (MS) ( $V_{\text{DMF}}:V_{\text{DMSO}} = 7:3$ ). The spin

coating of  $\text{PbI}_2$  solution on the ZnO NRs ( $\sim 870$  nm) was carried out at 5000 rpm for 30 s. The  $\text{PbI}_2$  film was then formed on ZnO nanorods by a two-step annealing at  $40^\circ\text{C}$  for 5 min, and  $100^\circ\text{C}$  for 10 min. After being cooled down to room temperature, the sample was dipped into the MAI solution (MAI was dissolved in 2-propanol under stirring at a concentration of 10 mg/mL) for 1 min. Consequently, the  $\text{MAPbI}_3$  perovskite layer was produced by thermal annealing (TA) or solvent annealing (SA) treatment at  $100^\circ\text{C}$  for 5 min. The hole transporting layer (HTM) was deposited by spin-coating the spiro-OMeTAD solution at 4000 rpm for 30 s. Finally, 80 nm of gold was deposited by thermal evaporation on the top of the devices as the back contact [5].

### 2.2. Materials characterization and performance evaluation of solar cells

All the devices area is  $0.3\text{ cm} \times 0.3\text{ cm}$ . The measurement of current-voltage curves was carried out under AM 1.5G simulated sunlight (Newport Oriel Sol3A Simulator, calibrated with an NREL-calibrated Si solar cell) with a Keithley 2400 source meter instrument. The external quantum efficiency (EQE) measurements were performed employing a solar cell quantum efficiency measurement system (QEX10, made by PV Measurements, USA) with a dual grating monochromator with computer control. Surface morphology of perovskite films was obtained using field emission SEM (FEI-Inspect F50, Holland). The X-ray diffraction (XRD) measurements were performed using a Bede D1 system with  $\text{Cu K}\alpha$  radiation. The UV–vis absorption spectra of ZnO NRs/perovskite films were measured using an ultraviolet–visible (UV–vis) spectrophotometer (Schimadzu UV-3101 PC). Electrochemical impedance spectroscopy (EIS) measurements were performed using electrochemical workstation (chi660d). The applied voltage perturbation had an AC amplitude of 35 mV (rms) with a frequency from 1 MHz to 100 Hz. The impedance parameters were simulated by fitting of the impedance spectra using Zview software. Transient photoluminescence (PL) spectra of the samples were measured using a Fluorolog-3 (Jobin Yvon Inc) fluorescence spectrophotometer to observe the recombination rate of photo-generated carriers.

## 3. Results and discussion

The pinholes and grain boundaries are known as the reasons for

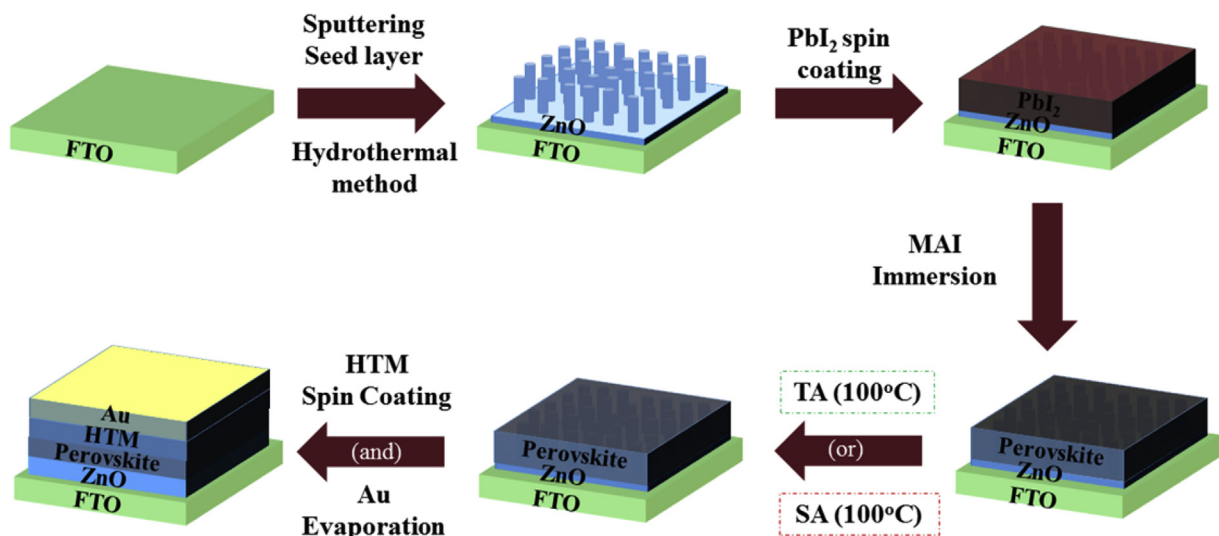


Fig. 1. Schematic flow diagram for fabrication of ZnO based PSCs.

poor photovoltaic performance of PSCs. It is therefore highly desired to increase the crystallinity of MAPbI<sub>3</sub> films. We firstly carried out two-step annealing for the PbI<sub>2</sub> films to investigate the crystallization. As shown in Fig. 2 (a)–(c), we deposited the PbI<sub>2</sub> films by spin-coating of a solution containing PbI<sub>2</sub> in a DMF, DMSO and MS solvent on ZnO NRs, respectively. The PbI<sub>2</sub> films produced from the DMF solution showed crystal grains, but with a very rough surface. The surface morphologies of PbI<sub>2</sub> films prepared by the pure DMSO solution display some pinholes because of their amorphous structure. It is interesting to see that PbI<sub>2</sub> films produced from the MS solution are porous.

It is well known that the DMF based lead halide crystallizes very quickly, and hence crystal grains are observed. DMSO molecules have stronger binding energy with Pb<sup>2+</sup>, and release slowly even under the annealing condition. For this reason, the lead halide in pure DMSO hardly crystallize, and the DMSO based PbI<sub>2</sub> film is amorphous. The two-step annealing process does not affect the formation of PbI<sub>2</sub> based on DMF and DMSO. But for the MS based solution case, the lower temperature annealing may result in precipitation of PbI<sub>2</sub> due to slow evaporation of solutions so that crystal grains increase slowly. Right after spin-coating, the PbI<sub>2</sub> films are wet with solvent. There still are many PbI<sub>2</sub> molecules or clusters in the solution. The preliminary crystal grains are formed at the lower temperature annealing in the first step. In the second step, the remaining solvent is removed quickly at the higher temperature. The solubility of PbI<sub>2</sub> depends on the strength of interaction between Pb<sup>2+</sup> and electronegative atoms [27]. DMSO molecules indicate stronger binding ability with Pb<sup>2+</sup> than that of DMF, and thus DMF released more quickly. Because DMSO molecules attach to the DMF solvent and are bond to Pb<sup>2+</sup> ion tightly, the DMSO-PbI<sub>2</sub> complexes exist until the beginning of high temperature (100 °C) annealing in the second step. The high temperature annealing induced the release of DMSO from the PbI<sub>2</sub> film, leading to formation of a mesoporous structure.

As shown in Fig. 2 (d), we observed colors of PbI<sub>2</sub> films based on different solvents changed from pale yellow to yellow. This further confirms the above discussion. The DMF based PbI<sub>2</sub> film showed the fastest rate of color change, suggesting the fastest crystallization rate of PbI<sub>2</sub>. By contrast, PbI<sub>2</sub> has the highest solubility in DMSO. Pb<sup>2+</sup> tends to have stronger interaction with sulfoxide oxygen in DMSO solution, which produces a more stable DMSO-PbI<sub>2</sub> complex. DMSO based PbI<sub>2</sub> films showed the slowest rate of color change, indicating that DMSO obviously retarded the crystallization of PbI<sub>2</sub> [20–22].

Fig. 3 (a)–(c) shows the surface SEM images of perovskite films fabricated from TA process. Based on the TA process, the MS based MAPbI<sub>3</sub> film exhibits the largest grain size, and the grains are evenly distributed on the surface. The average grain size of DMF based MAPbI<sub>3</sub> film is larger than that obtained from DMSO, which is consistent with the size distribution of crystal grains on the DMF based PbI<sub>2</sub> film. The smallest grain size of DMSO based MAPbI<sub>3</sub> film should be ascribed to the retarded crystallization. Compared with the TA process, the SA process increased the grain size of perovskite films produced from different PbI<sub>2</sub> films, as shown in Fig. 3 (d)–(f). Ethanol solution possesses a good solubility for MAI. The SA process facilitates the interaction of MAI into PbI<sub>2</sub> crystals for fully reaction in ethanol vapor atmosphere, and enlarges the crystal size. The mesoporous PbI<sub>2</sub> assisted growth of the perovskite films with the largest grains. Meanwhile, the compactness of perovskite films treated by SA is also obviously improved. The interconnected pores offer channels for MAI solution, allowing complete reaction of PbI<sub>2</sub> with MAI. Meanwhile, the mesoporous PbI<sub>2</sub> film provides a large surface area to promote the conversion of the lead halide to the perovskite. The pores created by the release of the DMSO from MS provide needful space for the volume expansion occurring during the conversion reaction, resulting in a compact perovskite film. In contrast, the perovskite crystals obtained from DMSO based PbI<sub>2</sub> distribute discretely on the surface of the film. The SA process

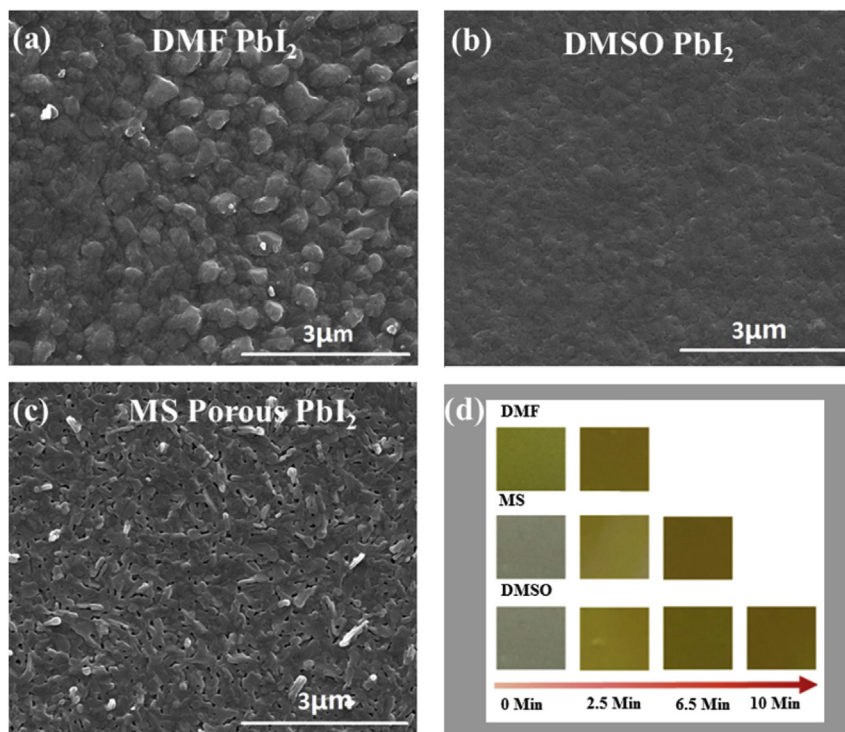
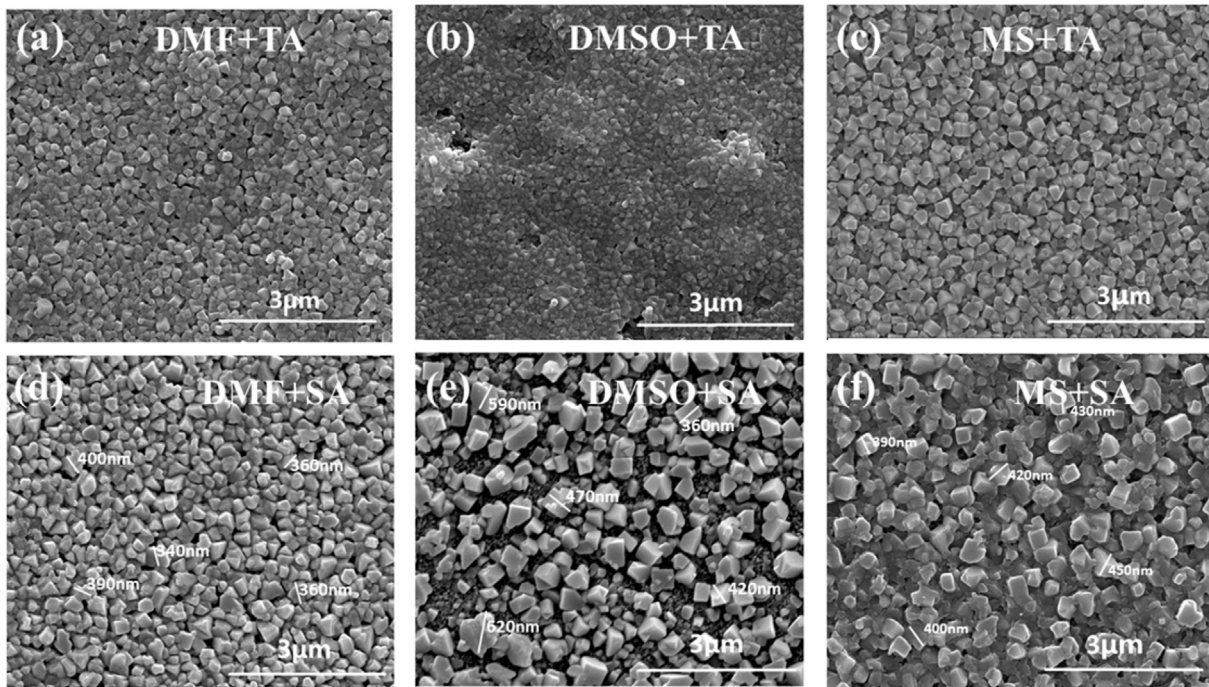


Fig. 2. (a), (b), and (c) surface morphology of PbI<sub>2</sub> films prepared with DMF, DMSO, and MS solution; (d) the color of different solvent based PbI<sub>2</sub> film exhibits from pale yellow to yellow for different annealing time. (For interpretation of the references to colour in this figure legend, the reader is referred to the web version of this article.)



**Fig. 3.** (a), (b) and (c), SEM morphology of DMF+TA, DMSO+TA, and MS+TA based perovskite films; (d), (e) and (f), SEM morphology of DMF+SA, DMSO+SA, and MS+SA based perovskite films.

increases the grain size of the DMF based perovskite film as well, but the grain size is much smaller than that of the MS based perovskite film. Therefore, we believe that the SA process enhances more effectively the grain size and compactness of the perovskite film based on mesoporous  $\text{PbI}_2$  than that based on DMF and DMSO.

We further evaluated the size of the SA treated perovskite crystals using software (Nano Measurer) as shown in Fig. S1. The DMF based  $\text{MAPbI}_3$  film exhibits the smallest average grain size of  $\sim 220$  nm, and the grain is evenly distributed on the surface. The average grain size of DMSO based  $\text{MAPbI}_3$  films is  $\sim 340$  nm, and the sizes are broadly distributed from about 100 to 500 nm. However, the mesoporous  $\text{PbI}_2$  based perovskite films have an average grain size of  $\sim 410$  nm and a small range of distribution, with more than 80% located in a small range around 300–600 nm.

As shown in Fig. 4 (a) and (b), a strong XRD peak ascribed to the remaining  $\text{PbI}_2$  is observed in the TA and SA treated  $\text{MAPbI}_3$  films based on DMF.  $\text{MAPbI}_3$  films based on DMSO show a much lower peak ascribed to  $\text{PbI}_2$ , and a weak XRD peak of  $\text{PbI}_2$  is shown in the MS based perovskite film. For DMF based  $\text{PbI}_2$  film, the fully crystallized  $\text{PbI}_2$  can react with MAI very quickly due to the easy intercalation of MAI into the lattice to form  $\text{MAPbI}_3$ . Such efficient reaction results in formation of crystallized  $\text{MAPbI}_3$  as a capping layer, which inhibits conversion of  $\text{PbI}_2$  under the capping layer to perovskite. The partial conversion of  $\text{PbI}_2$  leads to a  $\text{MAPbI}_3$ - $\text{PbI}_2$  mixture as well as a hardly controllable amount of remaining  $\text{PbI}_2$ . The residual  $\text{PbI}_2$  degrades the performance of solar cells owing to increase of the series resistance and decrease of optical absorption [20]. Consequently, we observed a strong XRD peak ascribed to the residual  $\text{PbI}_2$  in DMF based perovskite film. As we stated above, the mesoporous promotes the conversion of  $\text{PbI}_2$  to  $\text{MAPbI}_3$  by providing transporting channels and surface areas for MAI, resulting in negligible residual  $\text{PbI}_2$  in perovskite films. The full conversion of  $\text{PbI}_2$  to  $\text{MAPbI}_3$  is important for fabrication of highly reproducible PSCs.

The UV–vis spectrum of  $\text{MAPbI}_3$  films prepared by DMF based

$\text{PbI}_2$  as shown in Fig. 4 (c) displays an obvious peak at 510 nm ascribed to residual  $\text{PbI}_2$ . Meanwhile, the UV–vis spectrum shows that a pure  $\text{MAPbI}_3$  film prepared by MS based  $\text{PbI}_2$  films exhibits a stronger absorption at around 750 nm than that prepared by DMF based  $\text{PbI}_2$  films. By using ZnO NRs as ETM, we fabricated PSCs based on the TA process. The ZnO NRs were coated using three cycles of ALD- $\text{Al}_2\text{O}_3$ , and the defects on the surface were suppressed dramatically. The full scan XPS spectrum shown in Fig. S2 exhibits a weak, but distinct Al 2s peak at 125eV ascribed to ALD- $\text{Al}_2\text{O}_3$ , indicating that  $\text{Al}_2\text{O}_3$  monolayers were grown on ZnO NRs. The J–V curves of the TA treated PSCs are shown in Fig. 4 (d). The DMF, DMSO and MS based PSCs yields the PCE of 10.4%, 13.1%, and 15.6%. The results demonstrate that the crystallization and compactness of perovskite films dramatically influence the performance of PSCs. The MS based  $\text{MAPbI}_3$  film reveals uniformly continuous coverage on ZnO NRs, which offers an approach for high efficiency of 15.6%.

The high-resolution SEM cross section view of ZnO nanorods and corresponding PSC devices, and energy-level diagram of PSCs are shown in Fig. 5. The result indicates that the perovskite capping layer are formed on the ZnO NRs. Perovskite materials are filled tightly in the space between ZnO NRs. The photo-generated carriers in the perovskite film can be collected efficiently by ZnO ETM and Spiro-OMeTAD HTM. As shown in Fig. S3, the PSC based on ZnO NRs with the length of 870 nm exhibits the best efficiency (10.3%) among the PSCs with nanorods of different lengths. The following studies therefore are focused on the performance of PSCs based on ZnO NRs with the length of 870 nm.

We further employed the SA process on the DMF, DMSO, and MS based  $\text{MAPbI}_3$  films. The PSCs with SA treated perovskite films exhibit higher efficiency than the TA treated devices. As shown in Fig. 6 (a), the SA treatment on PSCs increases the PCE from 10.4% to 13.5%, from 13.1% to 14.7%, and from 15.6% to 17.3% separately. As stated above, the small average grain size results in large number of grain boundaries as well as large series resistance of PSCs because

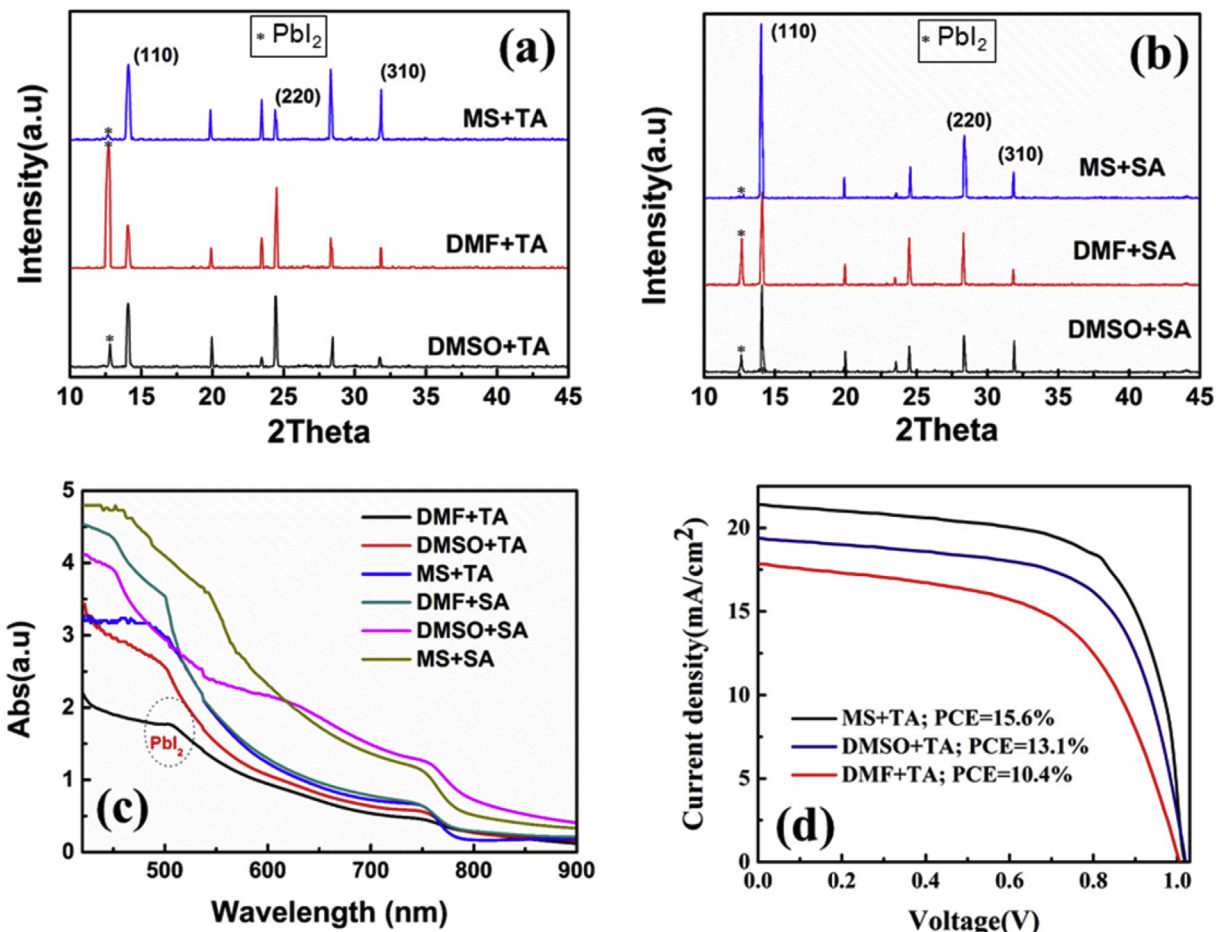


Fig. 4. (a) XRD patterns of DMF, DMSO, and MS based perovskite films treated by TA; (b) XRD patterns of DMF, DMSO, and MS based perovskite films treated by SA; (c) UV-vis absorption curve of DMF, DMSO, and MS based perovskite films; (d) J-V curves of DMF, DMSO, and MS based PSCs.

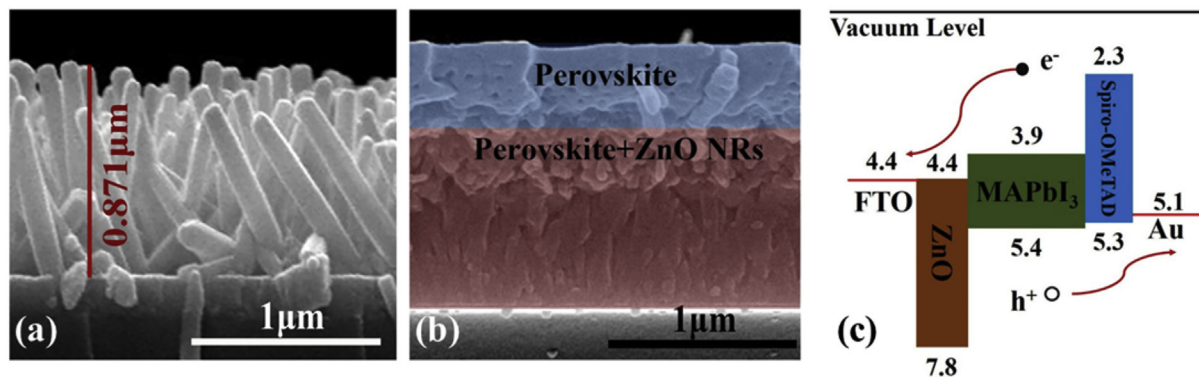
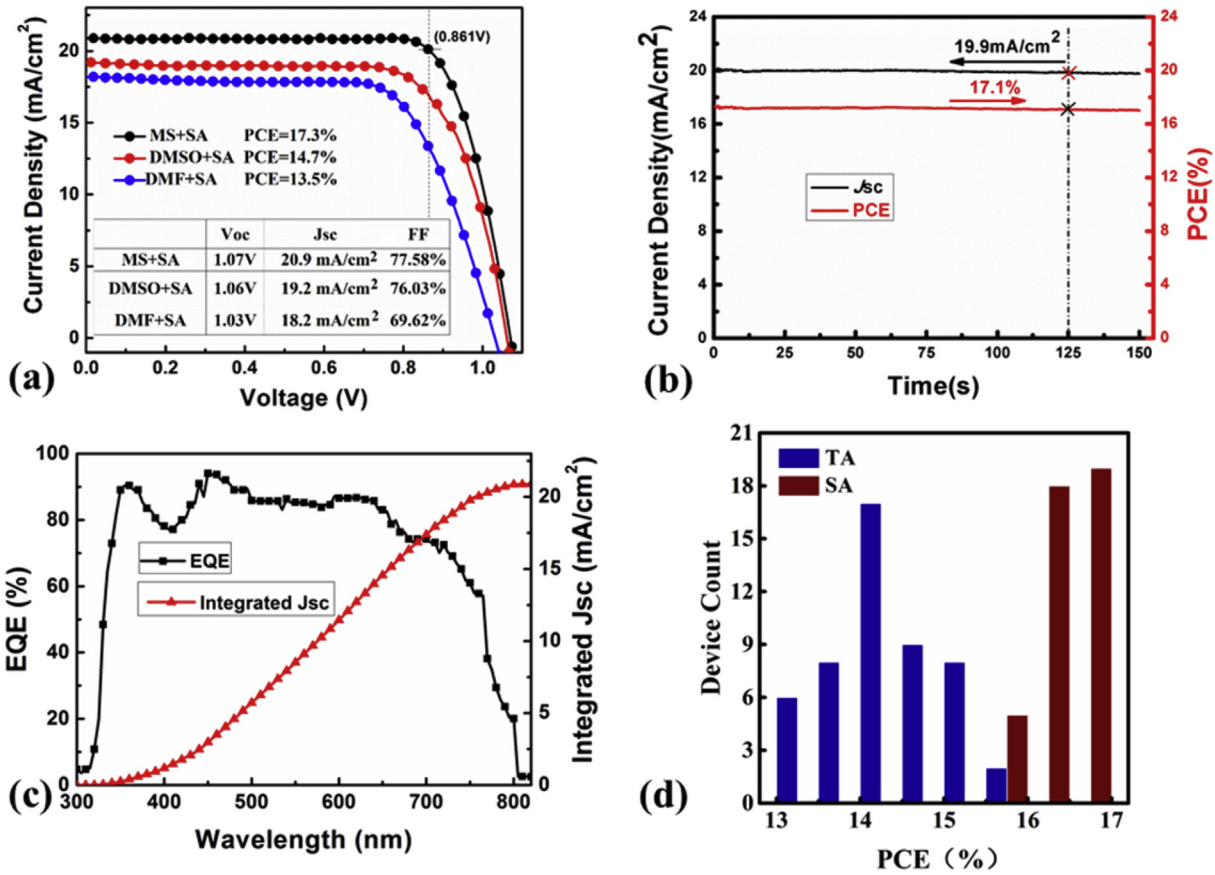


Fig. 5. (a) SEM cross section of ZnO NRs; (b) SEM cross section of perovskite films on ZnO NRs; (c) Energy level diagram of PSCs based on ZnO.

the photo-generated carriers have to cross more grain boundaries. In addition, the grain boundaries can act as scattering centers to reduce the lifetime of photo-generated electrons in the MAPbI<sub>3</sub> layer, which degrades the performance of PSCs [19]. For perovskite-based solar cells, the scan speed affects the J-V curves and the cause for this behavior is yet to be determined. A reliable, scan-independent metric to determine the efficiency of PSCs is the stabilized power output near the maximum power point. To identify the stable output, we measured the stable current density of the solar cells with a constant bias (0.861V) for 150s. As exhibited in

Fig. 6 (b), the stable current density is 19.9  $\text{mA}/\text{cm}^2$ , which is almost the same as that measured from the photocurrent scanning. The stable output PCE corresponding to the stable current density is 17.1%, represents the actual power output and efficiency. The external quantum efficiency (EQE) spectrum of the best sample is shown in Fig. 6 (c). The EQE demonstrates the onset of photocurrent at 800 nm, and high quantum yield throughout the entire wavelength range. Based on the EQE curve, we can calculate the short circuit current of the cell using the following equation:



**Fig. 6.** (a) *J*-*V* curves of the best PCE of DMF+SA, DMSO+SA, and MS+SA based PSCs; (b) Steady-state photocurrent output of the best PCE of MS+SA based solar device, measured at the maximum power point (0.861V); (c) EQE curve of the best performing MS+SA based solar device; (d) Reproducibility of TA and SA treated PSCs based on mesoporous PbI<sub>2</sub>.

$$J_{sc} = q \int_{\lambda_{min}}^{\lambda_{max}} P_{AM1.5}(\lambda) \cdot EQE(\lambda) d\lambda \quad (1)$$

Where  $q$  is the charge of electron,  $P_{AM1.5}(\lambda)$  is photon flux from the simulated sunlight.  $\lambda_{min}$  and  $\lambda_{max}$  are 300 and 800 nm, respectively. The spectrum is the same as that used to measure the PCE. The integrated photocurrent of 20.9 mA/cm<sup>2</sup> estimated from the EQE curve is in good agreement with that measured from IV characteristics shown in Fig. 6 (a). To investigate the reproducibility of PSCs, we fabricated two groups of PSCs based on mesoporous PbI<sub>2</sub> films. One group (50 devices) was treated by the TA process, and the other group (50 devices) was treated by the SA process. The efficiency distribution of both the TA and SA treated PSCs are shown in Fig. 6 (d) and summarized in Table 1. The average efficiency (14.34%) of the TA treated PSCs is lower than that of the SA treated PSCs (16.53%). The standard deviation of efficiency ( $\pm 0.677$ ) for the TA treated PSCs is significantly higher than that of the SA treated PSCs ( $\pm 0.393$ ). Both the average efficiency and the standard deviation of efficiency reveal that reproducibility of the SA based PSCs is greatly improved over that of the TA based PSCs. Due to the same

ZnO ETM and HTM layers used for all the PSCs, the enhanced average efficiency and reproducibility of SA based PSCs are ascribed to the optimized perovskite layer. The large and evenly distributed crystal size can be maintained in different individual devices because mesoporous PbI<sub>2</sub> assisted growth of fully converted perovskite.

EIS is a highly standard measurement technique to determinate the main electrical properties in devices' working conditions for a variety of inorganic and hybrid solar cells, including DSCs and quantum-dot sensitized solar cells [28–30]. As shown in Fig. 7 (a), the EIS measurements were performed at open circuit under one sun equivalent illumination. The Nyquist plots illustrate the discrimination of the charge transport and recombination at the FTO/ZnO/Perovskite/Spiro-OMeTAD/Au interface. Since no transmission line (TL) behavior is observed in this experiment, we simplified the circuit model. The resistance  $R_{con}$  can be obtained from the intersections of these arcs, corresponding to the resistance of the conducting glass, contacts and wires. The resistance  $R_{tr}$  from the high frequency arc regime mostly attributed to the transport resistance of ZnO/Perovskite/Spiro-OMeTAD layers. The total series resistance ( $R_{ser}$ ) of the device is equal to the sum of  $R_{con}$  and  $R_{tr}$ . The resistance from the low frequency arc is related to the

**Table 1**

Standard deviation of efficiency of TA and SA treated PSCs based on mesoporous PbI<sub>2</sub>, 50 devices were fabricated for each group.

	Device number	Standard deviation	PCE <sub>min</sub> [%]	PCE <sub>avg</sub> [%]	PCE <sub>max</sub> [%]
TA treatment	50	0.677	13.02	14.34	15.60
SA treatment	50	0.393	15.91	16.53	17.29

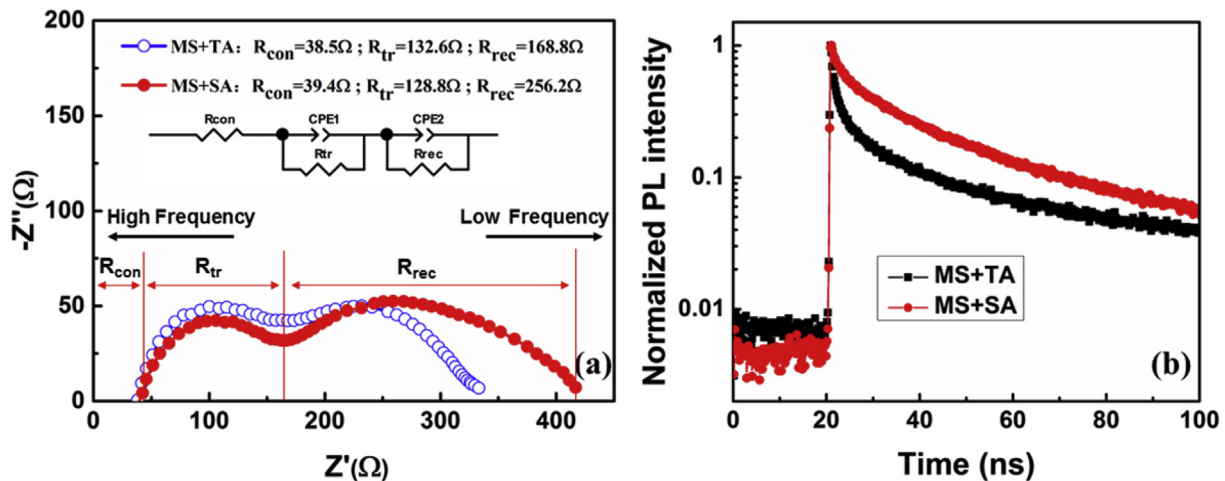


Fig. 7. (a) Electrochemical impedance spectra (EIS) of the devices measured at open circuit under one sun equivalent illumination; (b) Transient PL spectra of mesoporous based perovskite films.

recombination resistance,  $R_{rec}$ , mainly ascribed to the recombination of the electrons from perovskite with the holes. The carrier diffusion length,  $L_d$ , is given by Ref. [29].

$$L_d = \left( \frac{R_{rec}}{R_{tr}} \right)^{\frac{1}{2}} L \quad (2)$$

As the results shown in Fig. 7 (a), the TA and SA treatments of perovskite films influence weakly on the  $R_{tr}$ . Compared with the TA, the SA treatment of perovskite films obviously increases the value of  $R_{rec}$  in PSCs based on mesoporous  $\text{PbI}_2$ . The  $R_{rec}$  of the SA treated PSCs is 256.2  $\Omega$ , and the  $R_{rec}$  of the TA treated is 168.8  $\Omega$ . According to Equation (1), with similar  $R_{tr}$  and  $L$  in our prepared solar cells, there is no doubt that large  $R_{rec}$  in solar cells decreases the possibility for electron-hole recombination. This suggests that the increase of carriers diffusion length in perovskite is caused by the decrease of the grain boundaries and hole concentrations in  $\text{MAPbI}_3$  films. The SA treatment of perovskite films is important for obtaining long carrier diffusion length for effective charge collection in PSCs. As displayed in Fig. 7 (b), the transient PL spectra clearly demonstrate that the SA treatment improves the emission decay time in the perovskite films with large grain size [30]. The PL spectra further confirm that the compactness and large grains in perovskite films reduce grain boundaries and suppress carrier recombination.

#### 4. Conclusions

In summary, the mesoporous  $\text{PbI}_2$  films produced by the two-step annealing method assisted the growth of large perovskite grains. The crystallinity and grain size of perovskite films was further improved by SA process in ethanol vapor. SEM, XRD and UV absorption were carried out to elucidate the role of mesoporous  $\text{PbI}_2$  film and SA treatment in improvement of film crystallinity. The EIS and transient PL measurements confirm that the reported method reduces the grain boundaries and increases the carrier diffusion length as well as the recombination resistance in PSCs. The fabricated ZnO NRs based PSCs with high reproducibility yield high efficiency of 17.3%, which is the highest efficiency for ZnO based PSCs.

#### Acknowledgments

This work was supported by National Natural Science Foundation of China under Grant Nos. 61574029, 61371046, and 61421002, and National Higher-education Institution General Research and Development Fund (ZYGX2014J044). This work was also partially supported by University of Kentucky.

#### Appendix A. Supplementary data

Supplementary data related to this article can be found at <http://dx.doi.org/10.1016/j.jpowsour.2017.01.024>.

#### References

- [1] D. Zhao, M. Sexton, H. Park, G. Baure, J. Nino, F. So, *Adv. Energy Mater.* 5 (2015) 1401855.
- [2] Shibin Li, P. Zhang, H. Chen, Y. Wang, D. Liu, J. Wu, H. Sarvari, Z. Chen, *Nano Res.* (2016), <http://dx.doi.org/10.1007/s12274-016-1407-0>.
- [3] D. Zhao, W. Ke, C.R. Grice, A.J. Cimaroli, X. Tan, M. Yang, R.W. Collins, H. Zhang, K. Zhu, Y. Yan, *Nano Energy* 19 (2016) 88–97.
- [4] D. Liu, Shibin Li, P. Zhang, Y. Wang, R. Zhang, H. Sarvari, F. Wang, J. Wu, Z. Wang, Z.D. Chen, *Nano Energy* 31 (2017) 462–468.
- [5] J. Burschka, N. Pellet, S.J. Moon, R. Humphry-Baker, P. Gao, M.K. Nazeeruddin, M. Grätzel, *Nature* 499 (2013) 316–319.
- [6] A. Mei, X. Li, L. Liu, Z. Ku, T. Liu, Y. Rong, M. Xu, M. Hu, J. Chen, Y. Yang, Michael Grätzel, H. Han, *Science* 345 (2014) 6194.
- [7] S.D. Stranks, P.K. Nayak, W. Zhang, T. Stergiopoulos, H.J. Snaith, *Angew. Chem.* 54 (2015) 3240–3248.
- [8] D.Q. Bi, B. Xu, P. Gao, L.C. Sun, M. Grätzel, A. Hagfeldt, *Nano Energy* 23 (2016) 138–144.
- [9] X. Yin, J. Liu, J. Ma, C. Zhang, P. Chen, M. Que, Y. Yang, W. Que, C. Niu, J. Shao, *J. Power Sources* 329 (2016) 398–405.
- [10] N. Cheng, P. Liu, S. Bai, Z. Yu, W. Liu, S.S. Guo, X.Z. Zhao, *J. Power Sources* 321 (2016) 71–75.
- [11] Y. Jiang, H. Liu, X. Gong, C. Li, R. Qin, H. Ma, *J. Power Sources* 331 (2016) 240–246.
- [12] J. Yu, X. Chen, Y. Wang, H. Zhou, M. Xue, Y. Xu, P.D. Lund, *J. Mater. Chem. C* 4 (2016) 7302–7308.
- [13] Z.L. Tseng, C.H. Chiang, S.H. Chang, C.G. Wu, *Nano Energy* 28 (2016) 311–318.
- [14] REL Chart, 2016 (Accessed 13 June 2016), [http://www.nrel.gov/ncpv/images/efficiency\\_chart.jpg](http://www.nrel.gov/ncpv/images/efficiency_chart.jpg).
- [15] C. Liu, K. Wang, C. Yi, X.J. Shi, A.W. Smith, X. Gong, A.J. Heeger, *Adv. Funct. Mater.* 26 (2016) 101–110.
- [16] G. Longo, A. Pertegás, L. Martínez-Sarti, M. Sessolo, H.J. Bolink, *J. Mater. Chem. A* 3 (2015) 11286–11289.
- [17] Z. Liu, P. Luo, W. Xia, S. Zhou, J. Cheng, L. Sun, Y.W. Lu, *J. Mater. Chem. C* 4 (2016) 6336–6344.
- [18] Z.G. Xiao, Q.F. Dong, C. Bi, Y.C. Shao, Y.B. Yuan, J.S. Huang, *Adv. Mater.* 26 (2014) 6503.

- [19] D.S. Lee, W. Kim, B.G. Cha, J. Kwon, S.J. Kim, M. Kim, J. Kim, D.H. Wang, J.H. Park, *ACS Appl. Mater. Interfaces* 8 (2016) 449–454.
- [20] B. Wang, K.Y. Wong, S. Yang, T. Chen, J. Mater. Chem. A 4 (2016) 3806–3812.
- [21] H.D. Kim, H. Ohkita, H. Benten, S. Ito, *Adv. Mater.* 28 (2016) 917–922.
- [22] Q. Liang, J. Liu, Z. Cheng, Y. Li, L. Chen, R. Zhang, J. Zhang, Y. Han, *J. Mater. Chem. A* 4 (2016) 223–232.
- [23] J. Liu, C. Gao, X. He, Q. Ye, L. Ouyang, D. Zhuang, C. Liao, J. Mei, W. Lau, *ACS Appl. Mater. Interfaces* 7 (2015) 24008–24015.
- [24] J. Cao, F. Wang, H. Yu, Y. Zhou, H. Lu, N. Zhao, C. Wong, *J. Mater. Chem. A* 4 (2016) 10223–10230.
- [25] T. Liu, Q. Hu, J. Wu, K. Chen, L. Zhao, F. Liu, C. Wang, H. Lu, S. Jia, T. Russell, R. Zhu, Q. Gong, *Adv. Energy Mater.* 6 (2016) 1501890.
- [26] C. Yi, X. Li, J. Luo, S.M. Zakeeruddin, M. Grätzel, *Adv. Mater.* 28 (2016) 2964–2970.
- [27] Y. Wang, Shibin Li, P. Zhang, D. Liu, X. Gu, H. Sarvari, Z. Ye, J. Wu, Z. Wang, Z. Chen, *Nanoscale* 8 (2016) 19654.
- [28] A. Dualeh, T. Moehl, N. Tétreault, J. Teuscher, P. Gao, *Acs Nano* 8 (2013) 362.
- [29] V. Gonzalez-Pedro, E.J. Juarez-Perez, W.S. Arsyad, E.M. Barea, F. Fabregat-Santiago, I. Mora-Sero, J. Bisquert, *Nano Lett.* 14 (2014) 888.
- [30] S. Ye, W. Sun, Y. Li, W. Yan, H. Peng, Z. Bian, Z. Liu, C. Huang, *Nano Lett.* 15 (2015) 3723.